LETTER

doi:10.1038/nature22065

A 130,000-year-old archaeological site in southern California, USA

Steven R. Holen[1,2], Thomas A. Deméré[2], Daniel C. Fisher[3,4], Richard Fullagar[5], James B. Paces[6], George T. Jefferson[7], Jared M. Beeton[8], Richard A. Cerutti[2], Adam N. Rountrey[3], Lawrence Vescera[7] & Kathleen A. Holen[1,2]

The earliest dispersal of humans into North America is a contentious subject, and proposed early sites are required to meet the following criteria for acceptance: (1) archaeological evidence is found in a clearly defined and undisturbed geologic context; (2) age is determined by reliable radiometric dating; (3) multiple lines of evidence from interdisciplinary studies provide consistent results; and (4) unquestionable artefacts are found in primary context[1,2]. Here we describe the Cerutti Mastodon (CM) site, an archaeological site from the early late Pleistocene epoch, where *in situ* hammerstones and stone anvils occur in spatio-temporal association with fragmentary remains of a single mastodon (*Mammut americanum*). The CM site contains spiral-fractured bone and molar fragments, indicating that breakage occured while fresh. Several of these fragments also preserve evidence of percussion. The occurrence and distribution of bone, molar and stone refits suggest that breakage occurred at the site of burial. Five large cobbles (hammerstones and anvils) in the CM bone bed display use-wear and impact marks, and are hydraulically anomalous relative to the low-energy context of the enclosing sandy silt stratum. ^{230}Th/U radiometric analysis of multiple bone specimens using diffusion–adsorption–decay dating models indicates a burial date of 130.7 ± 9.4 thousand years ago. These findings confirm the presence of an unidentified species of *Homo* at the CM site during the last interglacial period (MIS 5e; early late Pleistocene), indicating that humans with manual dexterity and the experiential knowledge to use hammerstones and anvils processed mastodon limb bones for marrow extraction and/or raw material for tool production. Systematic proboscidean bone reduction, evident at the CM site, fits within a broader pattern of Palaeolithic bone percussion technology in Africa[3–6], Eurasia[7–9] and North America[10–12]. The CM site is, to our knowledge, the oldest *in situ*, well-documented archaeological site in North America and, as such, substantially revises the timing of arrival of *Homo* into the Americas.

The CM site was excavated by palaeontologists from the San Diego Natural History Museum (SDNHM) in 1992–1993 in coastal San Diego County, California, USA[13] (Extended Data Fig. 1a). Mastodon fossils and cobbles (Fig. 1a) were found in a 20–30-cm-thick sandy silt bed (Bed E) that was contained within a 12-m-thick sequence of Pleistocene sediments. The stratigraphic section consists of multiple upward-fining sequences of silt and fine-grained sand deposited in a low-energy fluvial environment (Extended Data Fig. 1b, c, Supplementary Information 1, 2 and Supplementary Table 1). Other strata in the same fluvial sequence contained fossils of extinct land mammals (for example, dire wolf, horse, camel, mammoth and ground sloth).

The disarticulated partial skeleton of a young adult male mastodon, recovered over a 50-m^2 area from Bed E, consists of 2 tusks, 3 molars, 4 vertebrae, 16 ribs, 2 phalanges, 2 sesamoids and over 300 bone fragments (Extended Data Fig. 2 and Supplementary Table 5). One tusk was found lying horizontally, and the other was oriented vertically with the distal portion penetrating the underlying strata. Femora were represented by detached femoral heads and spiral-fractured diaphyseal fragments that had been broken while fresh[14] (Fig. 2 and Extended Data Figs 3a, b, 4a–e), whereas several fragile ribs and vertebrae were unbroken.

Two concentrations of spiral-fractured bone and broken molar fragments were delineated, each clustered around a separate andesite cobble (concentrations 1 and 2 (Fig. 1b, c)). Refitting bone fragments were found in concentration 1 (Fig. 1c), where both femoral heads lay adjacent to each other (Extended Data Fig. 3b). Three refitting fragments of a percussion-fractured upper molar included one large segment in each concentration, and a cusp fragment that was found halfway between (Fig. 1c). Pegmatite fragments, which were found in concentration 1, refit with a large pegmatite cobble (Fig. 3 and Supplementary Video 7). Refitting andesite fragments and an andesite cobble that refits with an andesite flake were found in concentration 2 (Fig. 3).

Extensive evidence of percussion on bone and molars is present (Fig. 1c, Extended Data Figs 4, 5 and Supplementary Videos 1–5). Fifteen out of the seventeen bone and molar fragments and flakes produced by percussion are concentrated around two andesite cobbles (CM-281 and CM-114) (Fig. 1c). Concentration 1 contains three cone flakes[11] (CM-195, CM-438a and CM-438b; Figs 1c, 2a), one impact flake (CM-236; Fig. 1c), one percussion-fractured bone fragment (CM-288; Extended Data Fig. 4a–e) and a percussion-modified molar segment preserving a bulb of percussion and flake scar (CM-286; Fig. 1c and Extended Data Fig. 5f, i). CM-288 also preserves anvil polish, as do two other cortical bone fragments (CM-329 and CM-255) that are part of five refitting fragments (Extended Data Fig. 4a, e–h and Supplementary Video 6). Concentration 2 contains one cone flake (CM- 230; Fig. 2b), one impact flake (CM-222; Fig. 2c), a bone fragment with a bulb of percussion (CM-101) and a refitting molar segment (CM-103). One molar impact flake (CM-9), found at the edge of concentration 2, exhibits enamel on the platform and a bulb of percussion (Extended Data Fig. 5a, b). A femoral diaphysis fragment (CM-340), found 3 m from concentration 1, exhibits a 57-mm-wide arcuate impact notch with a partially detached cone flake and a negative flake scar within the wall of cortical bone (Fig. 2d and Supplementary Video 4).

Use-wear and impact marks on five CM cobbles (Fig. 4 and Extended Data Fig. 5g, h, j–n) were compared with similar features produced on hammerstones and anvils that were used in bone breakage experiments (Extended Data Fig. 6 and Supplementary Information 5) and with those described in published studies[15,16]. Cobbles CM-281 (concentration 1) and CM-114 (concentration 2) are interpreted as anvils based on use-wear and their location within concentrations of stone and bone fragments (Fig. 1b). Anvil CM-281 exhibits jagged scars, Hertzian

[1]Center for American Paleolithic Research, 27930 Cascade Road, Hot Springs, South Dakota, USA. [2]Department of Paleontology, San Diego Natural History Museum, San Diego, California, USA. [3]Museum of Paleontology, University of Michigan, Ann Arbor, Michigan, USA. [4]Department of Earth and Environmental Sciences, University of Michigan, Ann Arbor, Michigan, USA. [5]Centre for Archaeological Science, School of Earth and Environmental Sciences, Faculty of Science Medicine and Health, University of Wollongong, Wollongong, New South Wales, Australia. [6]Geosciences and Environmental Change Science Center, United States Geological Survey, Denver, Colorado, USA. [7]Colorado Desert District Stout Research Center, California Department of Parks and Recreation, Borrego Springs, California, USA. [8]Department of Earth Science, Adams State University, Alamosa, Colorado, USA.

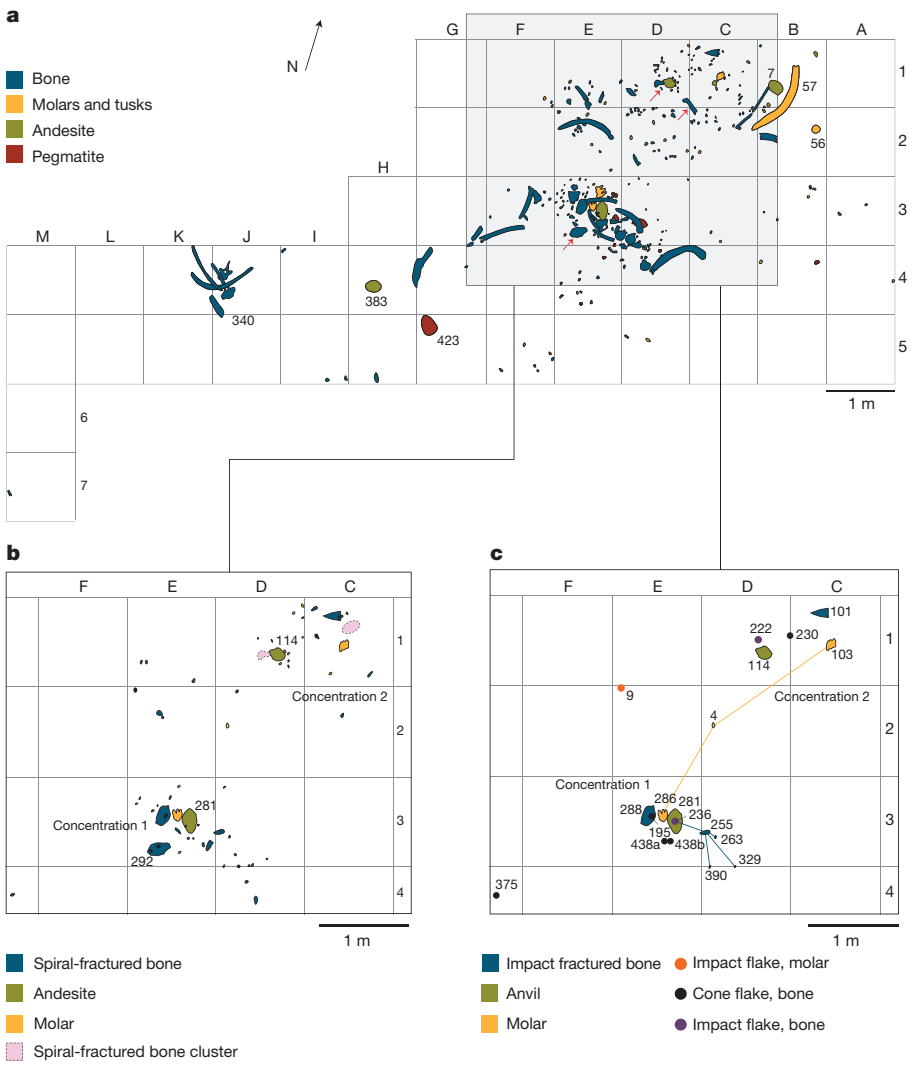

Figure 1 | Plan of the CM excavation site. a, Distribution of complete and fragmentary bones, teeth and cobbles. Note the circular cross-section of the tusk (CM-56) in grid unit B2. Red arrows indicate bones sampled for U–Th dating. **b**, Distribution of spiral-fractured bone, molar fragments and andesite anvils (CM-281, CM-114) in concentrations 1 and 2. **c**, Distribution of impact-fractured bone, cone flakes, impact flakes, bone refits and anvils in concentrations 1 and 2. Molar refits (yellow lines) were distributed between both concentrations. Bone refits (blue lines) were distributed between grid units D3 and E3. Cone flakes (CM-438a, CM-438b) that were found when screening grid unit E3 cannot be precisely plotted. Impact flake CM-236 was found above anvil CM-281.

initiations, step terminations, abrasion and striations in two areas along the upper surface indicating hammerstone blows (Fig. 4a–d). One lithic impact flake (CM-221; Extended Data Fig. 5c–e) was excavated slightly above CM-281. The upper cortical surface of anvil CM-114 has a low degree of surface modification, abrasive smoothing and fine striations consistent with breaking bone. One pegmatite cobble (CM-423) and two andesite cobbles (CM-7 and CM-383) are interpreted as hammerstones, based on use-wear and impact marks (Supplementary Information 3) and refitting fragments. Cobble CM-383 exhibits negative flake scars, Hertzian initiations, deep cracks and angular fractures and (rarely) pitting with jagged and crushed stone debris (Fig. 4e–h)—all consistent with missed hammer blows that struck an anvil. One lateral cortical surface exhibits patches of abrasive smoothing, short, fine striations, low polish development and phenocrysts with rounded edges elevated above the finer-grained matrix (Fig. 4i). Cobble CM-423 refits with six fragments (Fig. 3 and Supplementary Video 7), including CM-254, having a surface that exhibits microscopic wear with fine striations, suggesting impact with bone. On the edge opposite refitted fragment CM-254, cobble CM-423 displays typical stone-on-stone impact marks with macroscopic pitting (Extended Data Fig. 5h). Percussion flake CM-141, which refits with hammerstone CM-7, exhibits a battered, rounded external platform edge (Extended Data Fig. 5l, m), suggesting impact on bone, and contrasts with sharper fractures and other impact features on the edge of CM-7 from where CM-141 was detached (Extended Data Fig. 5k, n). These fractures and platform features are typical of a hammerstone striking a stone anvil[15].

Multiple bone and molar fragments, which show evidence of percussion, together with the presence of an impact notch, and attached and detached cone flakes support the hypothesis that human-induced hammerstone percussion[6,17,18] was responsible for the observed breakage. Alternative hypotheses (carnivoran modification, trampling, weathering and fluvial processes) do not adequately explain the observed evidence (Supplementary Information 4). No Pleistocene carnivoran was capable of breaking fresh proboscidean femora at mid-shaft[19–21] or producing the wide impact notch[22]. The presence of attached and detached cone flakes is indicative of hammerstone percussion[6,23], not carnivoran gnawing[18] (Supplementary Information 4). There is no other type of carnivoran bone modification[21,24] at the CM site, and nor is there bone modification from trampling[22]. The differential preservation of fragile ribs and vertebrae rather than heavy limb bones argues against trampling and is consistent with selective breakage by humans. Although some thick cortical limb bone fragments display longitudinal

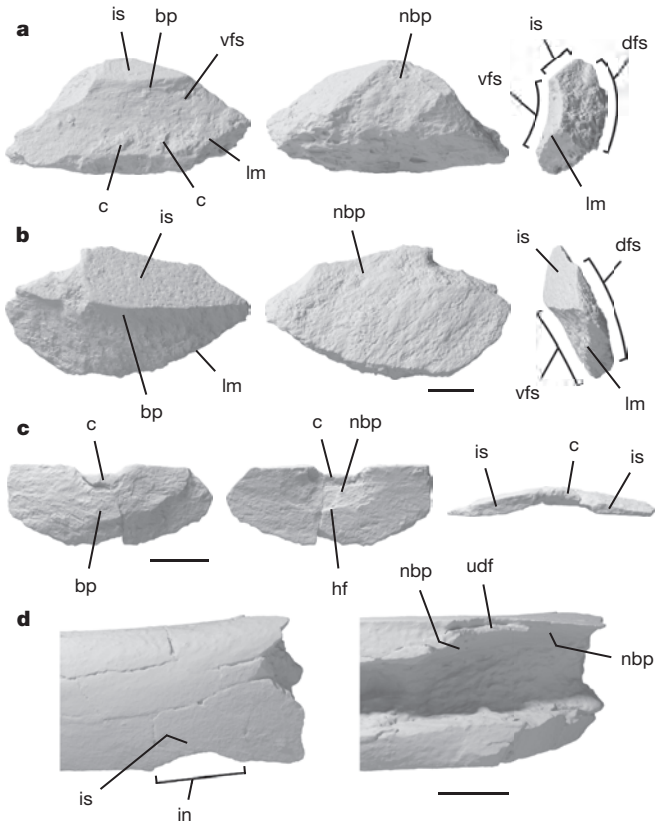

Figure 2 | Percussion-modified bone specimens (illustrated by 3D surface models). **a**, **b**, Cone flakes CM-438a (**a**) and CM-230 (**b**). From left to right the images show the ventral, dorsal and lateral views (as defined in lithic technology). **c**, Impact flake CM-222. From left to right the images show the ventral, dorsal and impact surface views. **d**, Femur fragment CM-340. Images show the cortical surface (left) and longitudinal section showing cortical bone thickness (right). bp, bulb of percussion; c, caliche remnant on bone surface; dfs, dorsal flake surface; hf, hinge termination; in, impact notch; is, impact surface; lm, lateral margin (ventral surface); nbp, negative bulb of percussion; udf, undetached flake; vfs, ventral flake surface. Impact surfaces that are external cortical surfaces are shown in **a**, **b**, **d**, whereas a fracture surface is shown in **c**. Scale bars, 1 cm (**a**–**c**) and 5 cm (**d**).

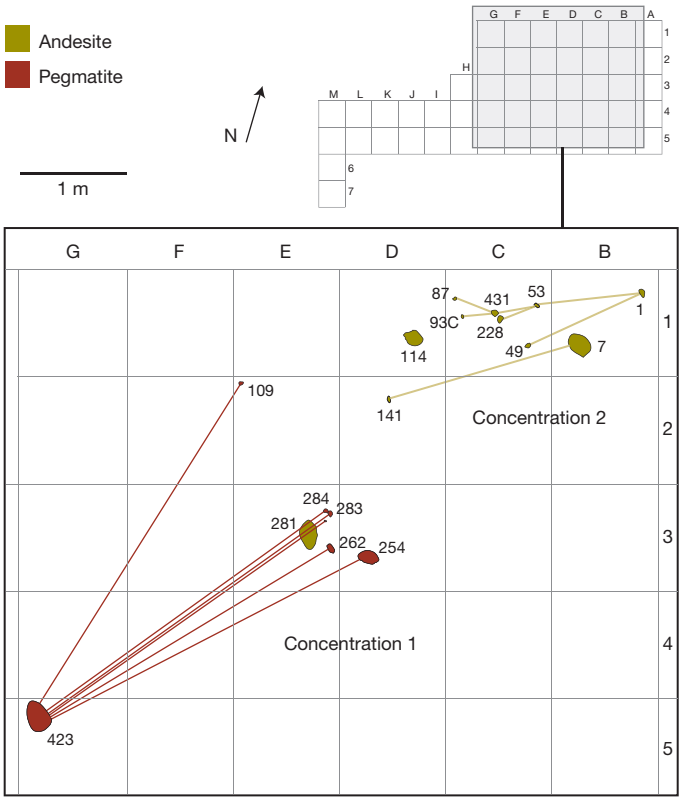

Figure 3 | Cobble refits. Distribution of rock refits (red and green lines indicate refits), hammerstones (CM-423 and CM-7) and anvils (CM-281 and CM-114). Note, rock refits CM-228 and CM-431 in concentration 2 were found when screening matrix from grid unit C1 and cannot be precisely plotted.

cracks and breaks, these features occurred after percussive bone modification (for example, impact events) and were caused by pre-burial factors (for example, subaerial weathering[25]) or by post-depositional factors (for example, wetting–drying cycles within the soil zone). The occurrence of large and small bones together with five large cobbles within an otherwise sandy silt horizon indicates that fluvial processes did not transport these bones and stones[26] (Supplementary Information 1, 2, 4 and 6). Spiral-fractured femoral fragments and both femoral heads adjacent to cobble CM-281 (Fig. 1a and Extended Data Fig. 3a, b) indicate that both femora were broken in that location. The vertical tusk (CM-56; Extended Data Figs 3c, 7c) is interpreted as the result of purposeful placement.

Fracture patterns and impact damage found on CM limb bones are consistent with results of experimental replication of Palaeolithic proboscidean bone percussion technology using hammerstones and anvils to fracture elephant[27] and cow femora (Extended Data Fig. 8a–d; Supplementary Information 5). Breakage patterns like those recorded at the CM and other archaeological sites were produced experimentally (Supplementary Information 5 and Supplementary Video 8), as was anvil polish (Extended Data Fig. 9a–d). During three experiments, hammerstones accidently struck a stone anvil and produced breakage features like those on hammerstones CM-383 and CM-423 (Supplementary Information 5).

The taphonomic pattern of the CM bone bed also differs from that of skeletons of horse and dire wolf discovered in adjacent strata within the same Pleistocene fluvial stratigraphic sequence (Extended Data Fig. 7a, b, Supplementary Information 6 and Supplementary Tables 2–9). These skeletons are more complete, do not show evidence of spiral fractures or percussion impacts and do not occur in association with cobbles.

Initial attempts to date the CM site using radiocarbon analysis at two independent laboratories failed, because the samples lacked sufficient collagen[13]. Several attempts to date the site with optically stimulated luminescence indicated that samples were near or beyond the upper limits of dose saturation, and that the depositional age of the sediment is greater than 60–70 thousand years (kyr) (Supplementary Information 7). Subsequently, multiple bone fragments (Extended Data Fig. 9e–g) were analysed by uranium-series disequilibrium methods (Methods and Supplementary Information 8). Profiles consisting of 13, 20 and 30 subsamples of cortical material across 12–23-mm-thick sections of two spirally fractured limb bones and one rib yielded consistent ∪-shaped patterns for both U-concentrations and conventionally calculated ^{230}Th/U ages (Extended Data Fig. 10a). These patterns are consistent with scenarios of post-burial U-uptake by diffusion and adsorption[28,29] and yield apparent closed-system ^{230}Th/U ages ranging from 100 to 107 kyr for interior subsamples and 112 to 125 kyr for subsamples from exterior cortical layers (Extended Data Fig. 10a, b and Supplementary Table 12). Initial ^{234}U/^{238}U activity ratios calculated for bone subsamples span a narrow range (1.38–1.50) that is consistent with modern shallow groundwater from the nearby Sweetwater River drainage (1.45–1.54; Supplementary Table 12) providing increased confidence in the ^{230}Th/U ages. Results calculated using diffusion–adsorption–decay[30] modelling for profiles of multiple specimens (Extended Data Fig. 10c) indicate a burial age estimate of 130.7 ± 9.4 kyr (weighted mean of three maximum-likelihood ages determined for bone profiles; Extended Data Fig. 10d). Isotope data are consistent with diffusion of U into interior

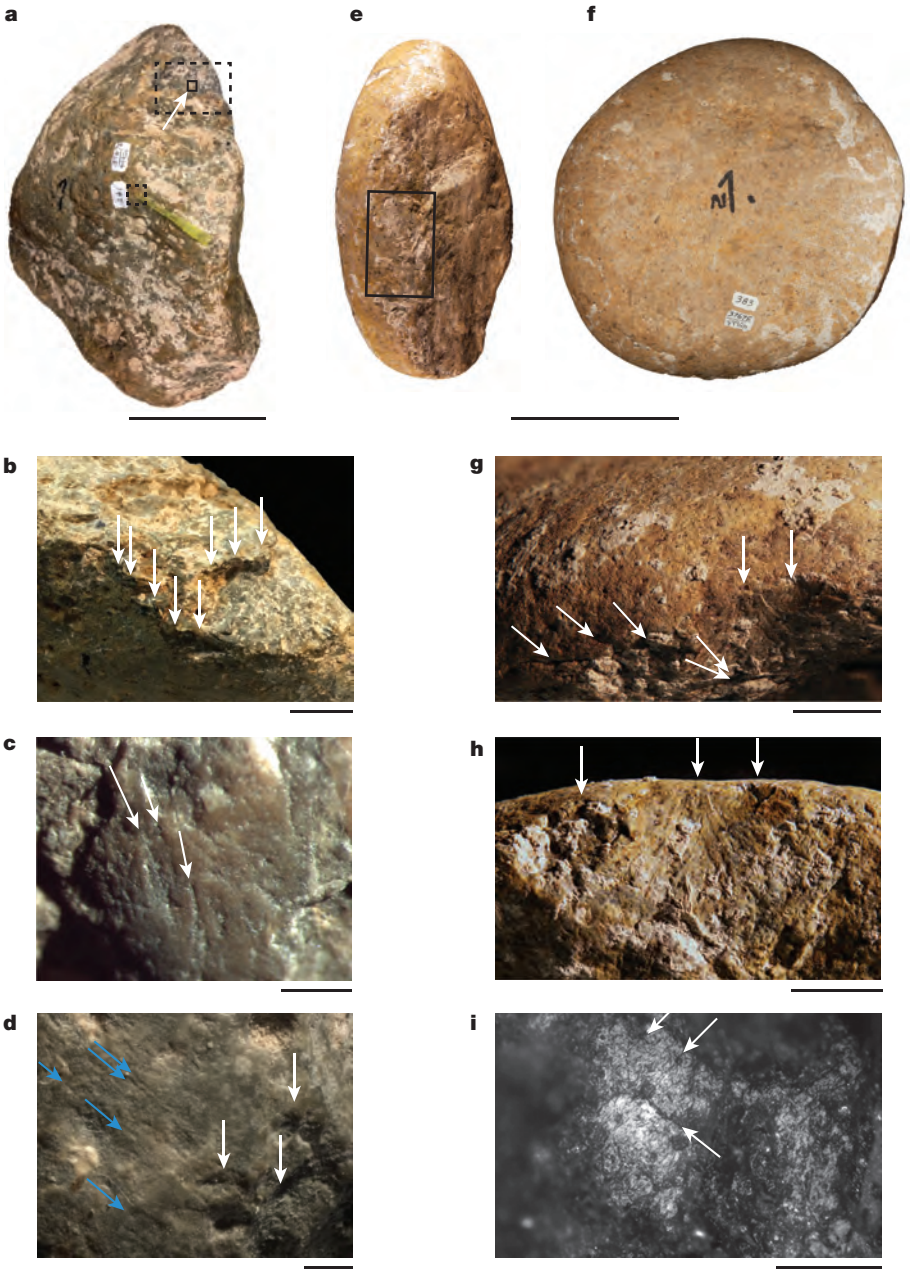

Figure 4 | Diagnostic impact marks. a–d, Anvil (CM-281). **a**, Upper surface. Boxes indicate images magnified in **b–d**; dashed rectangle, magnified in **b**, small dashed square, magnified in **c** and solid square, magnified in **d**. **b**, Cortex removal and impact marks (arrows). **c**, Striations (arrows) on the highest upper cortical surface ridge. **d**, Striations (diagonal arrows) and impact marks with step terminations characteristic of hammer blows (vertical arrows). **e–i**, Hammerstone (CM-383). **e**, Impact marks. The box indicates the magnified images in **g** and **h**. **f**, Upper smoothed surface. **g**, Deep cracks and impact scars (arrows). **h**, Impact scars from **g**, showing results of three discrete hammerstone blows on an anvil (arrows). The large flake scar (central arrow) has a clear point of impact with radiating fissures. The small scar (right arrow) has a negative impact cone and associated scars and fissures preserved beneath a layer of caliche. **i**, Striations (arrows) and abrasive polish on upper cortical surface (near black North arrow in **f**). Scale bars, 5 cm (**a**), 2 cm (**b**, **g**, **h**), 1 mm (**c**, **i**), 2 mm (**d**), 10 cm (**e**, **f**).

portions of cortical bone and show no obvious evidence for post-burial U leaching that would yield erroneously old ages (Supplementary Information 8).

We conclude that the reliably dated Cerruti Mastodon site constitutes an *in situ* archaeological association based on: a clearly defined and undisturbed stratigraphic context; comparative taphonomy; bone modifications like those produced by Palaeolithic percussion technology and replicated by experimental archaeology; presence of hammerstones and anvils that exhibit use-wear and impact marks; and presence of rock fragments that can be refitted to breakage scars. Bone breakage for marrow extraction and/or bone and molar tool manufacture is the preferred archaeological interpretation of the CM site, as there is no evidence of butchery. Concordant interdisciplinary lines of evidence from this study suggest the presence of *Homo* in North America during the last interglacial (MIS 5e) and as early as approximately 130 thousand years ago (ka) (Supplementary Information 9). This discovery calls for further archaeological investigation focused on North American strata of early late Pleistocene age.

Online Content Methods, along with any additional Extended Data display items and Source Data, are available in the online version of the paper; references unique to these sections appear only in the online paper.

Received 17 March 2016; accepted 13 March 2017.

1. Haynes, C. V. Jr. The earliest Americans. *Science* **166,** 709–715 (1969).
2. Stanford, D. J. in *Early Man in the New World* (ed. Shutler, R. Jr) 65–72 (Sage Publications, 1983).
3. de Heinzelin, J. *et al.* Environment and behavior of 2.5-million-year-old Bouri hominids. *Science* **284,** 625–629 (1999).
4. Leakey, M. D. *Olduvai Gorge. Vol. 3. Excavations in Beds I and II 1960–1963* (Cambridge Univ. Press, 1971).
5. Backwell, L. R. & d'Errico, F. The first use of bone tools: a reappraisal of the evidence from Olduvai Gorge, Tanzania. *Palaeont. Afr.* **40,** 95–158 (2004).
6. Domínguez-Rodrigo, M. *et al.* On meat eating and human evolution: a taphonomic analysis of BK4b (Upper Bed II, Olduvai Gorge, Tanzania), and its bearing on hominin megafaunal consumption. *Quat. Int.* **322–323,** 129–152 (2014).
7. Zutovski, K. & Barkai, R. The use of elephant bones for making Acheulian handaxes: a fresh look at old bones. *Quat. Int.* **406,** 227–238 (2016).
8. Gaudzinski, S. *et al.* The use of Proboscidean remains in every-day Palaeolithic life. *Quat. Int.* **126–128,** 179–194 (2005).
9. Ono, A., Orikasa, A. & Nakamura, Y. Palaeolithic bone tools from the 10th excavation season at Tategahana, Lake Nojiri, central north Japan. *Quat. Res.* **29,** 89–103 (1990).
10. Hannus, L. A. in *Megafauna and Man: Discovery of America's Heartland* (eds Agenbroad, L., Mead, J. & Nelson, L.) 86–99 (Scientific Papers 1 Mammoth Site of Hot Springs, 1990).
11. Johnson, E. Mammoth bone quarrying on the late Wisconsinan North American grasslands. in *The World of Elephants* 439–443 (2001).
12. Fisher, D. Mastodon butchery by North American Paleo-Indians. *Nature* **308,** 271–272 (1984).
13. Deméré, T. A., Cerutti, R. A. & Majors, C. P. *State Route 54 Paleontological Mitigation Program: Final Report* (San Diego Natural History Museum, 1995).
14. Johnson, E. in *Advances in Archaeological Method and Theory* Vol. 8 (ed. Schiffer, M. B.) 157–235 (Academic, 1985).
15. de la Torre, I., Benito-Calvo, A., Arroyo, A., Zupancich, A. & Proffitt, T. Experimental protocols for the study of battered stone anvils from Olduvai Gorge (Tanzania). *J. Archaeol. Sci.* **40,** 313–332 (2013).
16. Yustos, P. S. *et al.* Production and use of percussive stone tools in the Early Stone Age: Experimental approach to the lithic record of Olduvai Gorge, Tanzania. *J. Archaeol. Sci. Rep.* **2,** 367–383 (2015).
17. Pickering, T. R. & Egeland, C. P. Experimental patterns of hammerstone percussion damage on bones: implications for inferences of carcass processing by humans. *J. Archaeol. Sci.* **33,** 459–469 (2006).
18. Capaldo, S. D. & Blumenschine, R. J. A quantitative diagnosis of notches made by hammerstone percussion and carnivore gnawing on bovid long bones. *Am. Antiq.* **59,** 724–748 (1994).
19. Haynes, G. Frequencies of spiral and green-bone fractures of ungulate limb bones in modern surface assemblages. *Am. Antiq.* **48,** 102–114 (1983).
20. Morlan, R. E. *Taphonomy and Archaeology in the Upper Pleistocene of Northern Yukon Territory: A Glimpse of the Peopling of the New World* (Archaeological Survey of Canada, Paper No. 94, National Museum of Man, 1980).
21. Diedrich, C. J. Late Pleistocene Eemian hyena and steppe lion feeding strategies on their largest prey – *Palaeoloxodon antiquus* Falconer and Cautley 1845 at the straight-tusked elephant graveyard and Neanderthal site Newmark-Nord Lake 1, Central Germany. *Archaeol. Anthropol. Sci.* **6,** 271–291 (2014).
22. Lyman, R. L. *Vertebrate Taphonomy* (Cambridge Univ. Press, 1994).
23. Whiten, A., Schick, K. & Toth, N. The evolution and cultural transmission of percussive technology: integrating evidence from palaeoanthropology and primatology. *J. Hum. Evol.* **57,** 420–435 (2009).
24. Domínguez-Rodrigo, M. & Barba, R. New estimates of tooth mark and percussion mark frequencies at the FLK Zinj site: the carnivore-hominid-carnivore hypothesis falsified. *J. Hum. Evol.* **50,** 170–194 (2006).
25. Behrensmeyer, A. K. Taphonomic and ecologic information from bone weathering. *Paleobiology* **4,** 150–162 (1978).
26. Voorhies, M. *Taphonomy and Population Dynamics of an Early Pliocene Vertebrate Fauna, Knox County, Nebraska* (Contributions to Geology, Special Paper 1, Univ. Wyoming, 1969).
27. Holen, S. R. & Holen, K. in *IV Simposio Internacianal: El Hombre Temprano en America* (eds Jimenez Lopez, J. C., Serrano Sanchez, C., Gonzalez Gonzalez, A. & Aguilar Arellano, F. J.) 85–105 (Instituto Nacional de Anthropologia e Historia, 2012).
28. Millard, A. R. & Hedges, R. E. M. A diffusion-adsorption model of uranium uptake by archaeological bone. *Geochim. Cosmochim. Acta* **60,** 2139–2152 (1996).
29. Pike, A. W. G., Hedges, R. E. M. & Van Calsteren, P. U-series dating of bone using the diffusion-adsorption model. *Geochim. Cosmochim. Acta* **66,** 4273–4286 (2002).
30. Sambridge, M., Grün, R. & Eggins, S. U-series dating of bone in an open system: the diffusion–adsorption–decay model. *Quat. Geochronol.* **9,** 42–53 (2012).

Supplementary Information is available in the online version of the paper.

Acknowledgements The following individuals worked at the CM site: L. Agenbroad (deceased), B. Agenbroad, J. Mead, M. Cerutti, M. Colbert, C. P. Majors, B. Riney, D. Swanson (deceased) and S. Walsh (deceased). M. Hager was instrumental in ensuring completion of this project. J. Berrian and D. Van der Weele photographed bone and rock specimens and K. Johnson (SDNHM), S. Donohue (SDNHM), C. Abraczinskas (UMMP) and E. Parrish produced various main and Extended Data Figures. E. Hayes, J. Field and V. Rots assisted with photography and interpretation of use-wear on cobbles. C. Musiba and K. Alexander provided photographs of the experimental elephant bone breakage. E. Duke provided the photographs of the experimental anvil wear on bone. Financial support was provided by Caltrans-District 11, P. Boyce and D. Fritsch, The James Hervey Johnson Charitable Educational Trust, The National Geographic Society (Research Grant 4971-93), The Walton Family Foundation (at the recommendation of J. and C. Walton) and the many donors to the Center for American Paleolithic Research. Any use of trade, firm or product names is for descriptive purposes only and does not imply endorsement by the US Government.

Author Contributions R.A.C. discovered the CM site and led the excavation team. T.A.D. and S.R.H. conceived the study. S.R.H., T.A.D., K.A.H., R.A.C., D.C.F. and G.T.J. analysed the mastodon bone modifications. R.A.C., T.A.D., S.R.H., K.A.H. and D.C.F. identified refits of bones and cobbles. R.F. conducted the lithic use-wear analysis. J.M.B. and T.A.D. conducted the geological and soils analysis. J.B.P. conducted the U-series dating. D.C.F. provided mastodon skeletal identifications and analyses. G.T.J. and L.V. conducted the comparative taphonomic analysis. D.C.F. and A.N.R. produced the 3D models and videos of bone and cobbles. S.R.H., K.A.H. and R.F. conducted the experimental elephant, cow and kangaroo bone breakage. S.R.H., T.A.D., D.C.F., R.F., J.B.P., G.T.J., J.M.B. and K.A.H. wrote the paper with contributions by all other co-authors.

Author Information Reprints and permissions information is available at www.nature.com/reprints. The authors declare no competing financial interests. Readers are welcome to comment on the online version of the paper. Publisher's note: Springer Nature remains neutral with regard to jurisdictional claims in published maps and institutional affiliations. Correspondence and requests for materials should be addressed to T.A.D. (tdemere@sdnhm.org) or S.R.H. (sholen@goldenwest.net).

Reviewer Information *Nature* thanks E. Hovers and the other anonymous reviewer(s) for their contribution to the peer review of this work.

METHODS

Discovery and excavation of the Cerutti Mastodon site. The CM site (SDNHM locality 3767) was discovered during routine palaeontological monitoring of grading operations for construction of a sound-berm along the north side of State Route 54 in San Diego, San Diego County, California, USA. Palaeontological monitors from the San Diego Natural History Museum (SDNHM) observed mastodon bone and tooth fragments being unearthed in a distinct sandy silt stratum (Bed E, Extended Data Fig. 1b) by a Caterpillar 235C backhoe. This stratum extended to the south beneath the sound-berm. Numerous taphonomic anomalies (for example, vertical tusk, sharply broken bones and several large lithic clasts in a silt matrix) led to the establishment of a one-metre excavation grid to control material recovery and site mapping (Fig. 1a). Initially, the portion of Bed E impacted by backhoe excavation was carefully processed to remove all displaced fossils and cobbles. The backhoe did not disturb all of Bed E in the northern grid units (B1, C1, D1, E1, B2, C2 and D2)[13] and many fossils and the few cobbles in these units remained *in situ*. Bed E in other grid units remained intact and buried more deeply by overlying strata. Each grid unit was then excavated by hand, and all bone and cobble specimens larger than 2 cm were left *in situ*, mapped and labelled. All positional information was recorded, and each plotted specimen was assigned a unique CM site number. Once documented, bones, teeth and cobbles were excavated, removed with adhering matrix and transported to the SDNHM. One dense concentration of bones, tusk and cobbles found in portions of grid units B1, B2, C1 and C2 was excavated *en masse* in a plaster jacket. Excavation of the site generally proceeded from north to south. After grid units A3, B3 and C3 were completed the original grid was expanded into the sound-berm, adding six more columns (H–M) and one row (row 4). After grid units H3 and H4 were completed the grid was again expanded, adding one complete row (row 5) and two partial rows (6 and 7). Eventually the back wall of the excavation was up to 3 m high between the base of Bed E and the top of the sound-berm. All of the matrix in the Bed E portion of each grid unit was excavated and wet-screened through nested 0.84-mm and 0.59-mm-mesh stainless steel sieves to retrieve small faunal elements and small lithic fragments. A total of approximately 7,300 kg of Bed E matrix was processed in this manner.

A slightly modified one-by-one-metre grid excavation method was employed during recovery of other fossil vertebrates discovered in underlying strata (Bed D) exposed by construction activities. These included a partial horse skeleton (SDNHM 47731) discovered at SDNHM locality 3677 (Extended Data Fig. 7a) and a partial dire wolf skeleton (SDNHM 49012) and deer skeleton (SDNHM49666) discovered at SDNHM locality 3698 (Extended Data Fig. 7b). At these sites, fossils were initially exposed across a nearly level cut surface with minimal remaining sedimentary overburden. Two grid axes (that is, baseline and meridian) were laid out, and a rigid one-by-one-metre frame subdivided into decimetres was used to guide hand excavation work. All faunal elements were exposed, plotted, labelled and then removed. Sediment from each grid unit was then wet-screened as described above.

Specimen preparation. Recovered specimens were cleaned and stabilized at the SDNHM palaeontology laboratory. Special preparation techniques were used for cobble and bone specimens, several of which were encased in pedogenic carbonate. Care was taken to avoid any marking of bone surfaces by preparation tools. Pedogenic carbonate often was removed intact, whereas uncemented matrix was removed in layers. Cemented matrix was removed with small chisels or pneumatic scribes. Gentle water washing and soft toothbrushes were used to clean some specimens. A synthetic lacquer (General Electric Glyptal)–acetone solution, as well as cyanoacrylate glue, was used to consolidate fragile bones and teeth. Either cyanoacrylate or white aliphatic glue was used to repair damaged specimens, and hydrocal dental plaster was used to bridge gaps.

Soil stratigraphy. Soil samples were collected from Beds D, E and F strata as preserved in a large columnar block recovered from grid unit G5 during the original excavation of the CM site and stored at SDNHM. Soil and sediment colour, structure, gravel percentage, consistence, texture, clay films, root and pore space characteristics and calcium carbonate stages were described using standard procedures and nomenclature[31,32]. A pipette analysis was completed at the Kansas Geological Survey Geoarchaeology and Palaeoenvironment Laboratory on samples collected in 3-cm increments from the top of Beds F, through E and into D (Extended Data Fig. 1c). Samples from Beds F and E were sent to National Petrographic Service Inc. for thin section preparation. Thin section analysis was completed in the Adams State University (ASU) earth science laboratories using established procedures[33]. X-ray diffraction was also conducted at ASU using a benchtop Rigaku Mini Flex 600 on both air-dried and ethelyne-glycol-saturated samples of Bed E sediments[34].

Analyses of skeletal remains. Skeletal remains of the mastodon (SDNHM 49926) were examined to confirm element identifications and determine sex and age. The presence and type of bone surface modifications and breakage features were assessed by independent reviewers and only confirmed if a consensus was achieved. Bone and tooth refits[13] were likewise confirmed by independent review. Taphonomic anomalies including the vertical tusk fragment, side-by-side femoral heads, patterned bone fragment distributions and differential bone breakage were checked in original site photographs, field records and by examination of curated specimens[13] (documents on file, SDNHM Department of Paleontology). Field maps were digitized to produce final specimen-distribution maps.

Comparative taphonomic analysis. To evaluate whether the taphonomic history of the mastodon partial skeleton from Bed E differs from that of the other large mammalian skeletal remains recovered from Bed D, skeletal element orientations and anatomical positions[26,35] were compared and analysed for the four mammalian skeletons, *Mammut*, *Canis*, *Equus* and *Odocoileus*. The azimuths (Supplementary Tables 6–8) of the long axes of complete or nearly complete large limb bones and dentaries from the skeletal scatters were measured from quarry maps[13]: *Equus* sp. (SDNHM 47731) from SDNHM locality 3677 (Extended Data Fig. 7a), *Canis dirus* (SDNHM 49012) and *Odocoileus* (SDNHM 49666) from SDNHM locality 3698 (Extended Data Fig. 7b) and *Mammut americanum* (SDNHM 49926) from SDNHM locality 3767 (Fig. 1a). For ribs and fragments greater than about 15 cm, the long axis was the proximodistal axis. Dimensions of each bone scatter were also taken from these figures.

Identifications of skeletal elements at each of these localities were determined by examination of curated SDNHM materials and reference to comparative material at the University of Michigan Museum of Paleontology (for *Mammut*, see http://umorf.ummp.lsa.umich.edu/wp/wp-content/3d/bonePicker.html?name=Buesching). These data were used to calculate per cent completeness for each skeleton and per cent completeness of skeletal subsections (cervical, thoracic and lumbar vertebral series; major limb elements and feet; Supplementary Tables 6–8). Comparable complete skeletal element counts for living *Canis* and *Equus*[36] and for *Mammut*[37] were obtained. These skeletal element completeness and skeletal subsection data were compared to standard Voorhies Group Numbers (VGN)[26] reflecting the relative fluvial transport susceptibility of individual, disarticulated skeletal elements (VGN I, immediately removed; VGN II, removed gradually and VGN III, lag deposit).

The *Mammut americanum* (SDNHM 3767/49926) skeletal scatter includes no major appendicular elements sufficiently intact for axis orientation measurements. However, the orientations of several ribs and rib fragments (>20 cm) were measured to estimate current flow direction. The long axis of curved ribs and the horizontal tusk were operationally identified as a chord between proximal and distal ends. These directional data, bone orientations and skeletal scatter directions (measured by protractor) were plotted on circular histograms. The resulting patterns were compared (Supplementary Information 6) and taphonomic differences/similarities identified.

Lithic use-wear analysis. Use-wear and impact damage on five cobbles (Fig. 4 and Extended Data Figs 5, 6) were compared with use-wear on experimental grinding/pounding tools, including our bone breakage experiments and published studies[15,16]. CM cobbles and other lithic fragments were inspected macro- and microscopically for traces of use. Refitting fragments previously identified (data on file, SDNHM palaeontology collections archives) were confirmed by independent review. Lithic fragment distributions were digitized and maps were generated using Adobe Illustrator. Worn surfaces of three cobbles (CM-254, CM-383 and CM-114) were examined with a Zeiss Axiotech microscope at magnifications of 50× to 500×, with vertical incident light (bright field, differential interference contrast) and polarizing filters. Images were captured with a Zeiss HRc digital camera. Experimental hammerstones and CM-281 were examined under low magnification (6.7× to 45×) using an Olympus SZ61 stereomicroscope with an external fibre optic, 150-Watt halogen light source (Olympus LG-PS2) and a Leica MZ16A stereomicroscope with an automatic *Z*-stacking function. Multifocal images were obtained using a DFC320 Leica camera and stitched to create a focused image using Leica LAS v4.4 software. Cobble surfaces were also examined under high magnification using an Olympus metallographic microscope (model BH-2) with vertical incident light (bright field and dark field) at magnifications from 50× to 500×. Microscopic wear traces included the form and distribution of abrasive smoothing, polish, striations, crushing and fractures. Traces were compared with wear on naturally weathered cobbles and with use-wear on previously studied experimental tools used for various grinding and pounding tasks[38].

Experimental modern elephant and cow bone breakage. Results of two bone breakage experiments using elephant (*Loxodonta africana)* skeletal remains were compared with the breakage patterns present on CM bones. Elephants are the closest living relatives of mastodons and provide the best experimental proxy for extinct proboscidean remains. Both experiments replicated hammerstone percussion on fresh elephant limb bones and were recorded with video and still photography archived at the Center for American Paleolithic Research.

The first experiment, performed in Tanzania, documented breakage of a femur from an approximately 28-year-old male elephant that died of pneumonitis nine days before dissection. The femur was placed on a wooden anvil and fractured using a 4.3-kg andesite cobble hammer (which tapered to a 3 × 5 cm point) hafted onto a 1.2-m-long wooden handle (Extended Data Fig. 8a, c).

The second experiment (in Colorado, USA) used limb bones from a 46-year-old female zoo elephant that had been euthanized and buried in anoxic conditions for approximately three years preserving all soft tissue. Limb bones were well-preserved and behaved like fresh bone when percussed. A femur, tibia, fibula and humerus were placed in turn on a cobble anvil. An initial attempt using a 2.8-kg granite cobble hammer hafted onto an 81-cm-long wooden handle was unsuccessful because the hammer broke when it struck the anvil on the first blow. Subsequently, a 14.7-kg unhafted and unmodified gneissic granite cobble hammerstone that tapered to a point approximately 8 cm in diameter was used to impact the bone placed on a 17.3-kg granite cobble anvil (Extended Data Fig. 8b) and a 12.3-kg quartzite anvil.

One additional experiment was conducted using 15 cow (*Bos taurus*) femora that were broken using a hand-held 2.95-kg granite cobble hammerstone and the 17.3-kg granite cobble anvil used in the second elephant bone breakage experiment. Resulting bone breakage was documented using a digital SLR camera.

Breakage patterns and use-wear on elephant and cow bone from these experiments were examined macroscopically and microscopically. Photomicrography of experimentally produced anvil use-wear was conducted at the South Dakota School of Mines and Technology, USA, with a Leitz Z16 APO apochromatic microscope system with vertical incident light. Other macroscopic photographs of bones were taken with a Nikon D90 35 mm digital camera with an 18–55 mm lens or a Nikkor 105 mm macro lens.

Analyses of Cerutti Mastodon bone modifications. Bone modification characteristics, breakage patterns and bone fragment distributions were visually and graphically compared with the experimental bone modification made by hammerstone percussion and with proboscidean bone assemblages from known archaeological sites[10–12]. All bone elements and fragments were inspected for evidence of spiral (helical) fracturing, percussion marks and/or flaking. Specimens with these features were selected for further analyses.

Spiral-fractured specimens[14,39–41] were identified without prior knowledge of their location on the master CM site map, or their relation to the location of an anvil. The distributions of spiral-fractured mastodon bone fragments (Fig. 1b) were compared qualitatively with photographs of distributions of fragments around anvils used experimentally (Extended Data Fig. 8a, c). Evidence of percussion, cone flakes and impact notches with associated flake scars were identified according to published criteria[17,18,24].

Three-dimensional modelling of spiral-fractured bone and lithic specimens. Three-dimensional models of several CM specimens were generated photogrammetrically from sets of photographs taken inside a light-tent that illuminated specimens diffusely while minimizing shadows. This strategy optimizes feature-matching between different views of a specimen, improving the quality of the resulting three-dimensional model.

Photographs were taken with a Nikon D700, D70 or D810 digital SLR camera. Each specimen was documented with images taken from more than 130 unique orientations. Initial reconstruction used VisualSFM[42,43] (Windows x64 CUDA version 0.5.26) to calculate lens parameters and camera positions from photographs. Undistorted photographs and camera positions were then exported to CMPMVS[44], which produced the final 3D mesh. Resulting 3D models typically had several million faces, providing excellent resolution of the details. Models were scaled in Meshlab (http://meshlab.sourceforge.net/) using calliper measurements of original specimens. Owing to differences in lighting and white balance settings during photography of CM-383, the hue of the model was adjusted in Meshlab after reconstruction. One model (CM-340) was initially reconstructed using CMPMVS, but a second model with more detail was created using commercial photogrammetry software (RealityCapture, Capturing Reality s.r.o.).

The models are most effectively viewed dynamically in a custom viewer that can be found at http://umorf.ummp.lsa.umich.edu (search for 'Cerutti'; for refit assemblies, elements may be 'ghosted' by using the 'V' key (toggle to reverse) to examine details of fit that would otherwise be obscured by neighbouring fragments), but we offer brief animations (.mp4 files) of isolated fragments and refit assemblies in the Supplementary Videos. To facilitate viewing on the web, models were simplified to 2 million faces using Meshlab. Natural colour models use downsampled vertex colour data from CMPMVS[44]. Some models are presented in flat grey for better visualization of topography. Animations and stills for Fig. 2 were created using Blender (Blender Foundation).

Uranium-series dating. *Samples.* U-series isotope analyses were determined by thermal-ionization mass spectrometry (TIMS) at the USGS Denver radiogenic isotope laboratory on specimens collected and curated by the SDNHM. Initial attempts used specimens of bone (Spl.1 and SDNHM-09) from the initial backhoe excavation. Subsequent dating efforts focused on cortical-bone profiles from specimens of rib or limb bone found *in situ* from mapped areas of bone concentrations (CM-20, CM-225 and CM-292), including specimens with spiral fractures. Specimens were sectioned across the long axis of the bone and polished (Extended Data Fig. 9e–g). The degree of mineralization in cortical bone is high; however, low-U calcite filling micropores do not contribute appreciably to the isotopic composition of the high-U hydroxyapatite bone matrix. Dark-stained material (mostly Mn oxides) was avoided where possible; however, stained and unstained material yielded similar U–Th concentrations and isotope compositions.

Subsamples were obtained using carbide dental drills to collect 0.003–0.098 g of powder (median of 70 analyses = 0.0172 g). For cortical profiles, bone sections were mounted on a manually controlled milling stage. Subsampling proceeded sequentially from outer to inner surfaces (Extended Data Fig. 9e–g). Powdered material from each step was collected on glassine paper, and any remaining powder was removed under magnification using dissecting needles and compressed air.

Chemical separation. Samples were transferred to fluoropolymer vials, weighed, spiked with a mixed ^{236}U–^{233}U–^{229}Th tracer solution, and digested using ultra-pure 7 N nitric acid at 110 °C overnight. Solutions were dried, then redissolved in 7 N nitric acid. Purification of U and Th fractions used standard column chromatography with around 0.5 ml of AG1 × 8 resin and a sequence of 7 N nitric acid, followed by elution of Th using 6.5 N hydrochloric acid, and elution of U using 0.05 N nitric acid. Total process blanks ranged from 10–20 pg U and 20–100 pg Th.

Analytical measurement. Purified salts were loaded onto the evaporation side of double rhenium filament assemblies for U and onto single rhenium filaments sandwiched between layers of graphite suspension for Th. Isotope ratios of U ($^{234}U/^{235}U$, $^{236}U/^{235}U$, and $^{236}U/^{233}U$) and Th ($^{230}Th/^{229}Th$ and $^{232}Th/^{229}Th$) were determined in multi-dynamic peak-hopping mode on a Thermo Finnigan Triton TIMS equipped with a single discrete-dynode secondary electron multiplier and a retarding potential quadrupole (RPQ) filter that increased abundance sensitivity to better than 10 ppb. Measured $^{234}U/^{235}U$ and $^{236}U/^{235}U$ atomic ratios were corrected for mass fractionation using the known $^{236}U/^{233}U$ isotope ratio in the tracer solution.

Replicate analyses of U-isotope standard (NIST 4321B) yielded a mean $^{234}U/^{235}U$ atomic ratio of 0.007291 ± 0.000012 (2 standard deviations (s.d.) for 129 analyses), which is within error of the accepted value (0.007294 ± 0.000028). Corrections for instrument bias were made by normalizing $^{234}U/^{235}U$ values measured for unknowns by the same factor needed to adjust ratios measured for the SRM 4231B standard. Measured and calculated atomic ratios were converted to activity ratios (AR) using accepted decay constants[45,46], and the assumption that all U has an atomic $^{238}U/^{235}U$ composition of 137.88 (ref. 47). Replicate analyses of solutions of 69 million-year-old U ore[48] in radioactive secular equilibrium analysed in the same manner yielded a mean $^{234}U/^{238}U$ AR and $^{230}Th/^{238}U$ AR values of 1.0002 ± 0.0041 and 0.9996 ± 0.0081, respectively (2 s.d. for 20 analyses), both of which are within analytical uncertainty of the expected values of 1.000. Results for an in-house late Pleistocene *Acropora* coral dating standard[49] (age of 119.6 ± 1.9 ka) yielded an average age of 119.1 ± 3.3 ka (±2 s.d., $n = 23$) and an average initial $^{234}U/^{238}U$ AR value of 1.152 ± 0.005 (±2 s.d., $n = 23$), which is within uncertainty of accepted values for seawater[50] (1.150 ± 0.006).

All uncertainties for isotope ratios and associated data are given at the 95% confidence level and include within-run analytical errors based on counting statistics, external errors based on reproducibility of standards, and errors propagated from uncertainties assigned to the assumed detrital component and the amount of detrital material present in a given sample (negligible for all analyses of bone).

Data availability. The U–Th isotopic data that support the geochronological findings of this study are available in machine-readable form at USGS ScienceBase (https://www.sciencebase.gov/catalog/) with the DOI: 10.5066/F7HD7SW7.

31. Soil Survey Division Staff. *Soil Survey Manual* (US Department of Agriculture, 1993).
32. Birkeland, P. W. *Soils and Geomorphology* 3rd edn (Oxford Univ. Press, 1999).
33. Dyar, M. D. & Gunter, M. E. *Mineralogy and Optical Mineralogy* (Mineralogical Society of America, 2007).
34. Moore, D. M. & Reynolds, R. C., Jr. *X-ray Diffraction and the Identification and Analysis of Clay Minerals* 2nd edn (Oxford Univ. Press, 1997).
35. Toots, H. Orientation and distribution of fossils as environmental indicators. *Guidebook: Nineteenth Field Conference of the Wyoming Geological Association*, 219–229 (1965).
36. Sisson, S. & Grossman, J. D. *The Anatomy of the Domestic Animals* (W. B. Saunders and Co., 1953).

37. Fisher, D. C. in *Mastodon Paleobiology, Taphonomy, and Palaeoenvironment in the Late Pleistocene of New York State: Studies on the Hyde Park, Chemung, and North Java Sites* (eds Allmon, W. D. & Nester, P. L.) 197–290 (Paleontological Research Institution, 2008).
38. Fullagar, R. in *Archaeology in Practice: a Student Guide to Archaeological Analyses* 2nd edn (eds Balme, J. & Paterson, A.) 232–263 (Malden: Blackwell Publishing, 2014).
39. Outram, A. K. A new approach to identifying bone marrow and grease exploitation: why the "indeterminate" fragments should not be ignored. *J. Archaeol. Sci.* **28,** 401–410 (2001).
40. Hoffecker, J. F. *et al.* Evidence for kill-butchery events of early Paleolithic age at Kostenski, Russia. *J. Archaeol. Sci.* **37,** 1073–1089 (2010).
41. Karr, L. P. & Outram, A. K. Bone degradation and environment: understanding, assessing and conducting archaeological experiments using modern animal bones. *Int. J. Osteoarchaeol.* **25,** 201–212 (2015).
42. Wu, C. VisualSFM: A Visual Structure from Motion System. http://ccwu.me/vsfm/ (2011).
43. Wu, C. SiftGPU: A GPU Implementation of Scale Invariant Feature Transform (SIFT). http://cs.unc.edu/~ccwu/siftgpu (2007).
44. Jancosek, M. & Pajdla, T. Multi-view reconstruction preserving weakly-supported surfaces. *IEEE Conference on Computer Vision and Pattern Recognition* (CVPR, 2011).
45. Cheng, H. *et al.* Improvements in ^{230}Th dating, ^{230}Th and ^{234}U half-life values, and U–Th isotopic measurements by multi-collector inductively coupled plasma mass spectrometry. *Earth Planet. Sci. Lett.* **371–372,** 82–91 (2013).
46. Jaffey, A. H., Flynn, K. F., Glendenin, L. E., Bentley, W. C. & Essling, A. M. Precision measurements of half-lives and specific activities of ^{235}U and ^{238}U. *Phys. Rev. C* **4,** 1889–1906 (1971).
47. Steiger, R. H. & Jäger, E. Subcommission on geochronology: convention on the use of decay constants in geo- and cosmochronology. *Earth Planet. Sci. Lett.* **36,** 359–362 (1977).
48. Ludwig, K. R., Wallace, A. R. & Simmons, K. R. The Schwartzwalder uranium deposit, II: age of uranium mineralization and lead isotope constraints on genesis. *Econ. Geol.* **80,** 1858–1871 (1985).
49. Watanabe, Y. & Nakai, S. U–Th radioactive disequilibrium analyses for JCp-1, coral reference distributed by the Geological Survey of Japan. *Geochem. J.* **40,** 537–541 (2006).
50. Delanghe, D., Bard, D. & Hamelin, B. New TIMS constraints on the uranium-238 and uranium-234 in seawaters from the main ocean basins and Mediterranean Sea. *Mar. Chem.* **80,** 79–93 (2002).

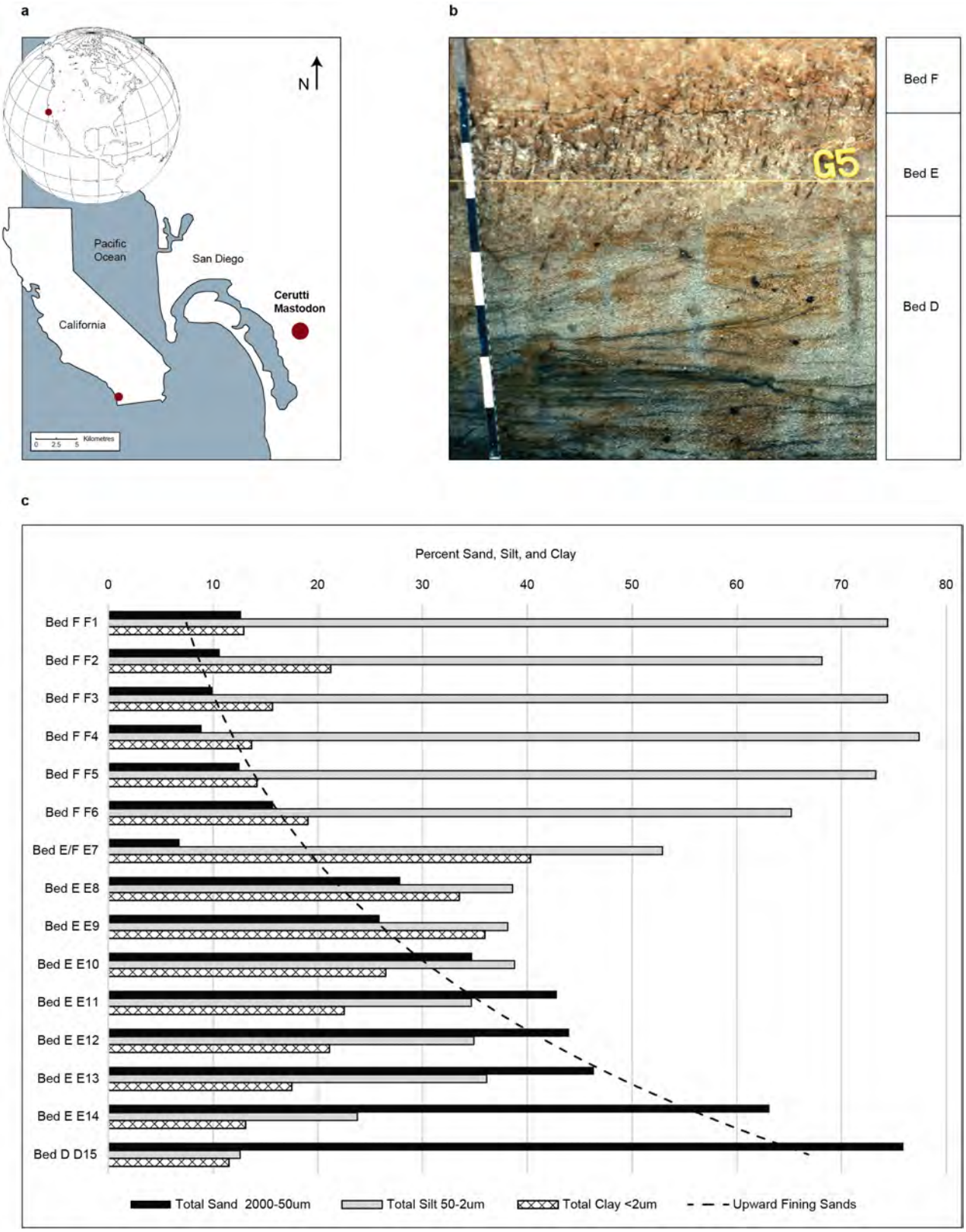

Extended Data Figure 1 | The CM site. a, Map of southwestern San Diego County, California, USA, showing the location of the CM site (red dot). Map created by E. Parrish using esri data and software. **b**, Stratigraphy of CM site: Bed D (C horizon; sandy loam; cross-bedded; fluvial), Bed E (Bk horizon; loam; fluvial) and Bed F (Bt horizon; loam; fluvial) as exposed in excavation grid unit G5. Contacts at Beds D–E and Beds E–F transitions are gradational. **c**, Total sand, silt and clay percentages from pipette analysis of 15 bulk samples collected in stratigraphic order showing a clear upward-fining sequence in 3 cm increments beginning in Bed D and continuing through Beds E and F. The clay percentage increases near the top of Bed F (Bt horizon) and Bed E (Bk horizon).

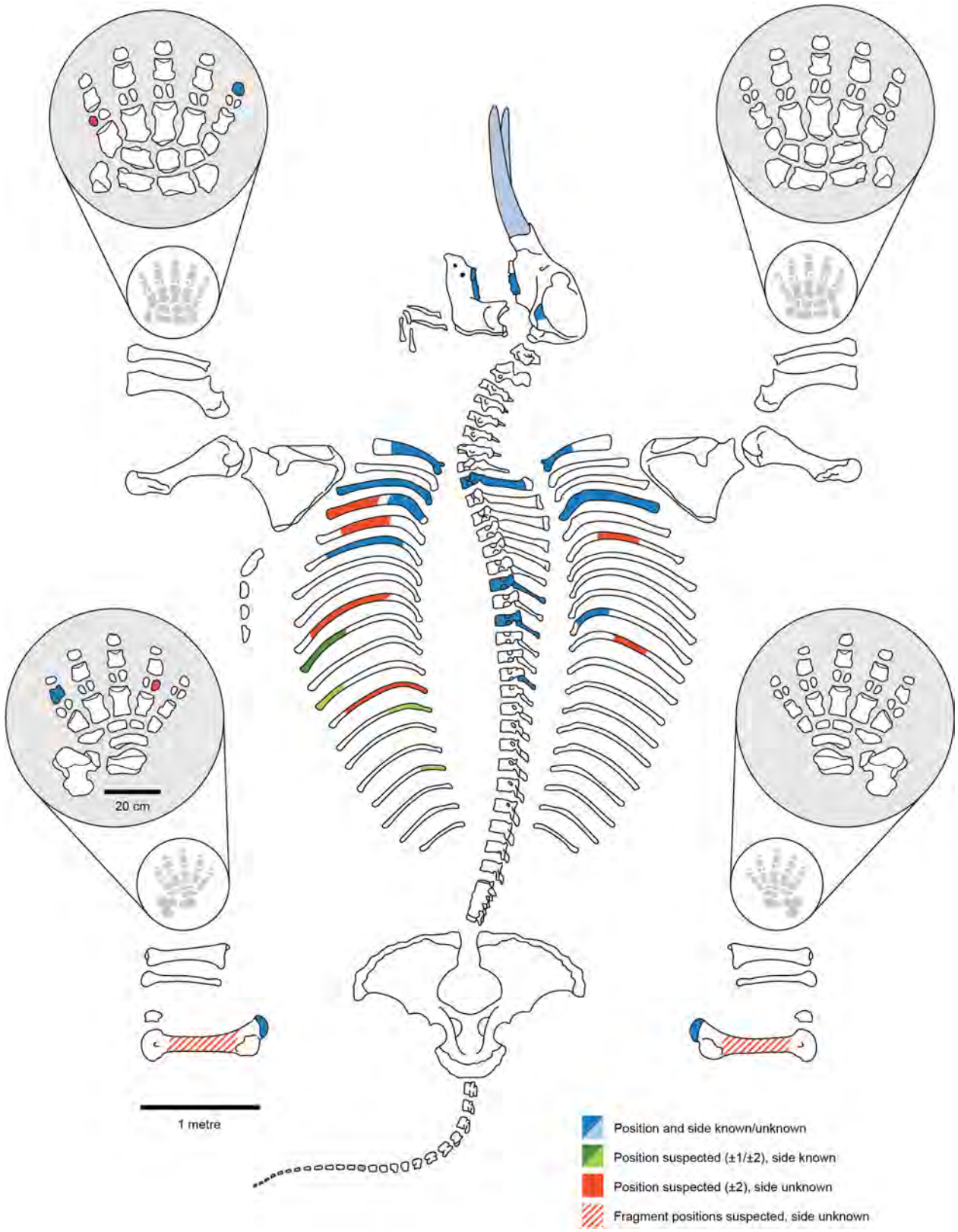

Extended Data Figure 2 | Schematic representation of *Mammut* skeletal elements. Most elements are shown in approximately lateral aspect, except for basihyoid (oblique), and manus and pes elements (most anterior, calcaneum dorsal). Coloured elements were sufficiently intact to determine their anatomical positions. Dark blue elements were determined with the greatest precision. Light blue elements were determined except for the side. Light green elements were determined with an uncertainty of ±2 positions within their respective series. Red elements were determined with an uncertainty of ±2 positions within their respective series, but the side was undetermined. Femoral diaphyses (red diagonal stripes) are the probable source of most cortical bone fragments showing conspicuous 'green fractures'.

Extended Data Figure 3 | Bones and cobbles exposed during excavation. **a**, Oblique view of concentration 1 in grid unit E3. Note the position of anvil CM-281, spirally-fractured femoral fragments CM-288 and CM-292 and molar fragment CM-286. **b**, Plan view of *in situ* femoral heads in grid units D3/E3. **c**, Plan view of vertical tusk in grid unit B2, showing cross-section of concentric dentin layers exposed by backhoe. **d**, Plan view of *in situ* caudal vertebra and rib in grid units D4 and E4. **e**, Plan view of portion of *in situ* rib (left) and hammerstone CM-383 (right) in grid unit H4. Note the carbonate 'rind' on CM-383. **f**, Oblique view of *in situ* hammerstone CM-423 in grid unit G5. Note the fine-grained aspect of Bed E containing CM-423.

Extended Data Figure 4 | Diagnostic anvil wear on CM bone. **a**–**e**, Spiral-fractured femur segment CM-288. **a**, V-shaped projection with anvil polish (rectangle). **b**, Side view with V-shaped projection. **c**, Outer, cortical surface. **d**, Side view with impact surface and bulb of percussion (highlighted with a black dashed line) on opposite side from anvil wear. **e**, Enlarged area from **a** showing impact fracture marks (arrows) where the bone rested on the anvil. **f**, Spiral-fractured V-shaped cortical bone CM-329 with anvil polish (oval). **g**. Spiral-fractured bone CM-255 that refits with CM-329 (white rectangle showing the location of the close-up shown in **h**). **h**, Enlarged area from **g** showing anvil striations. Scale bars, 2 cm (**a**), 5 cm (**b**–**d**), 5 mm (**e**), 10 mm (**f**–**h**).

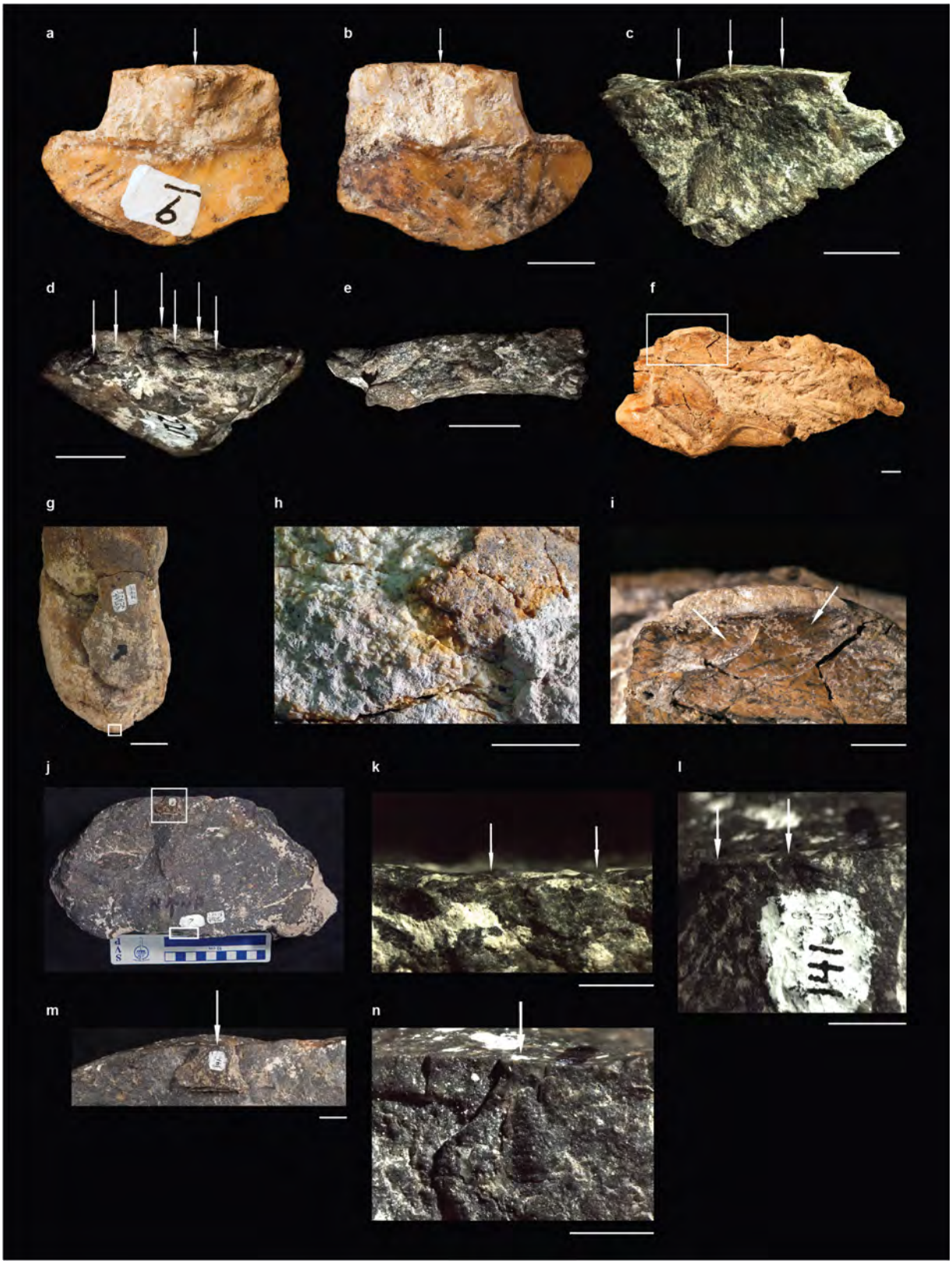

Extended Data Figure 5 | See next page for caption.

Extended Data Figure 5 | Percussion-caused features on molar and cobble specimens. a, **b**, Molar impact flake CM-9. **a**, Bulb of percussion (arrow). **b**, Negative flake scar (arrow). **c–e**, Andesite flake CM-221. **c**, Ventral view showing slight edge rounding on the proximal internal platform edge (arrows). **d**, Oblique dorsal view showing proximal dorsal scars (arrows) with step terminations. **e**, Platform view showing natural cortical surface and step-terminated scars. **f**, **i**, Molar segment CM-286. **f**, Cross-sectional view showing impact area (rectangle, magnified in **i**). **i**, Close-up of the impact area showing flake scar (left arrow) and bulb of percussion (right arrow). **g**, Fragment CM-262 refitted on fragment CM-254 with both refitted on pegmatite hammerstone CM-423. These fragments were probably dislodged by a blow to the end of CM-423 (square). **h**, End-on view of CM-423, showing pitting and cracks from the impact. Note that caliche covers the pitted area adjacent to zones where caliche covers the cortex. **j–n**, Andesite hammerstone CM-7 and impact flake CM-141 showing use-wear features. **j**, Upper surface of CM-7 showing refitted flake CM-141 (square, top) and a battered ridge (rectangle, bottom). **k**, Battered ridge on CM-7 (rectangle in **j**) with stone-on-stone impact scars (arrows) indicating the direction of blows. **l**, Detail of refitted flake CM-141 showing rounded external platform edge (left arrow) and older flake scar initiation (right arrow). **m**, Dorsal view of refitted flake CM-141 showing location and direction of impact (arrow) adjacent to fresh fracture scars of prior flake removals. **n**, Fresh fracture surface on andesite hammerstone CM-7 where flake CM-141 refits, showing fissures and cracks converging on the point of impact (arrow). Scale bars, 5 mm (**a–e**, **k–n**), 10 mm (**f**, **i**), 2 cm (**g**, **h**).

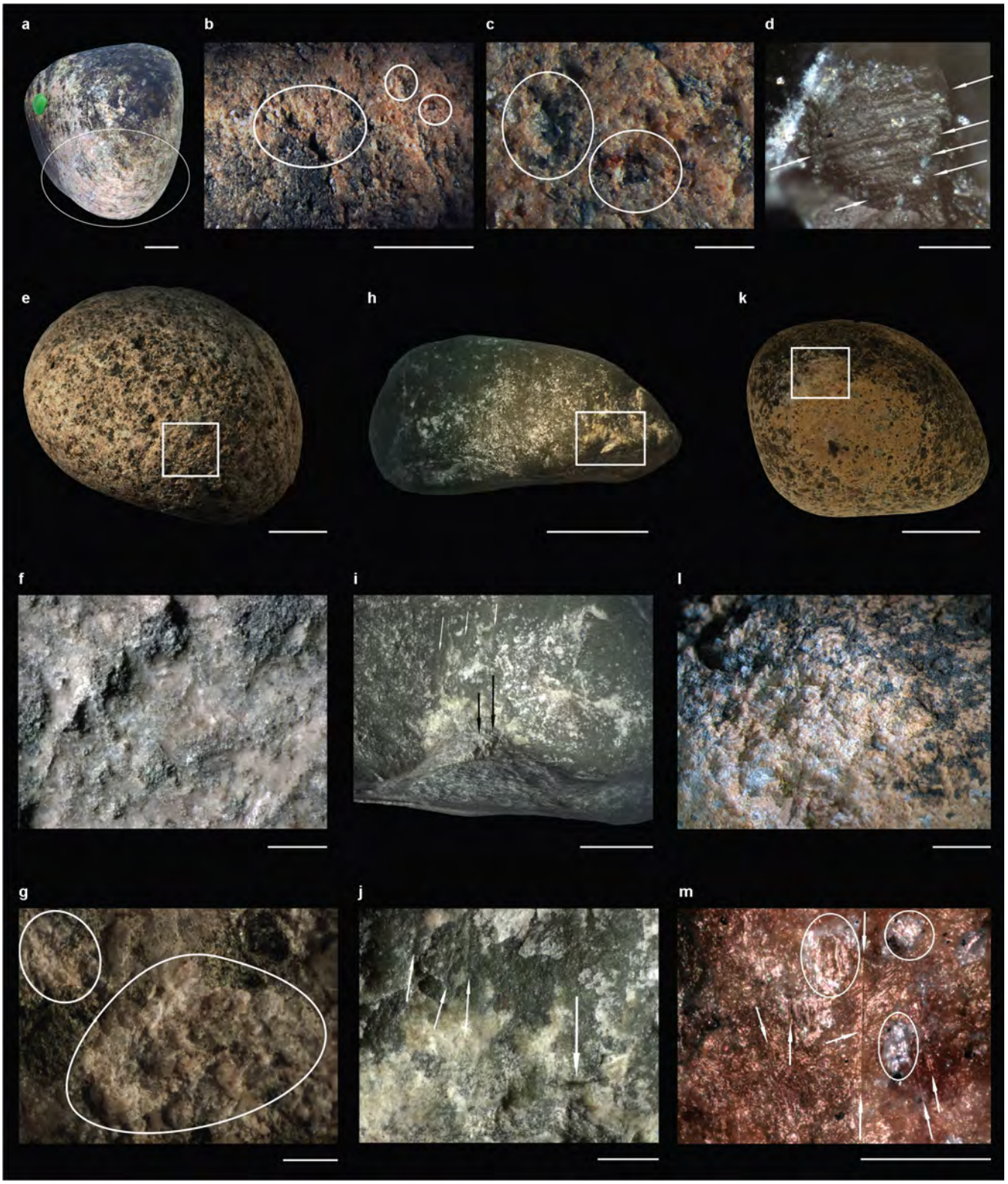

Extended Data Figure 6 | Wear on experimental bone pounding tools. **a**–**d**, Elephant experiment. **a**, Eight-cm wide tip of the experimental cobble hammerstone showing pitted zone (ellipse, magnified in **b**). **b**, Detail of use-wear in **a** showing pitted zones (ellipse and circles). **c**, Detail of use-wear shown in circles in **b**. **d**, Detail of use-wear (striations) on an individual quartz grain in the lower right circle in **c**. **e**–**j**, Cow experiment. **e**, Tip of the experimental granite cobble hammerstone showing pitted zone (square). **f**, Naturally weathered cortex of cobble shown in **e** away from any contact with bone. **g**, Detail of pitted area (in ellipses) on the experimental cobble in **e** showing angular quartz crystals, depressions/pits where crystals have been dislodged and white powdery cobble debris. **h**, Tip of argillite hammerstone showing pitted zones and fractures (square). **i**, Detail of striations (white arrows) and the impact fractures (black arrows) shown in **h**. **j**, Detail of striations (arrows pointing upward) above crushing and a step scar (arrow pointing downward). **k**–**m**, Kangaroo experiment. **k**, Granite cobble hammerstone showing impact and pitted zone (square, magnified in **l**). **l**, Detail of pitted zone from **k**. **m**, Striations (arrows) and abrasive smoothing/polish (flat whiter zones near striations) associated with pitted zones shown in **l**. Bone residues appear as lightly translucent white tissue (ellipses). Scale bars, 2 cm (**a**, **e**, **h**, **k**), 10 mm (**b**, **i**, **j**), 2 mm (**c**), 1 mm (**f**, **g**), 5 mm (**l**), 500 μm (**d**), 100 μm (**m**).

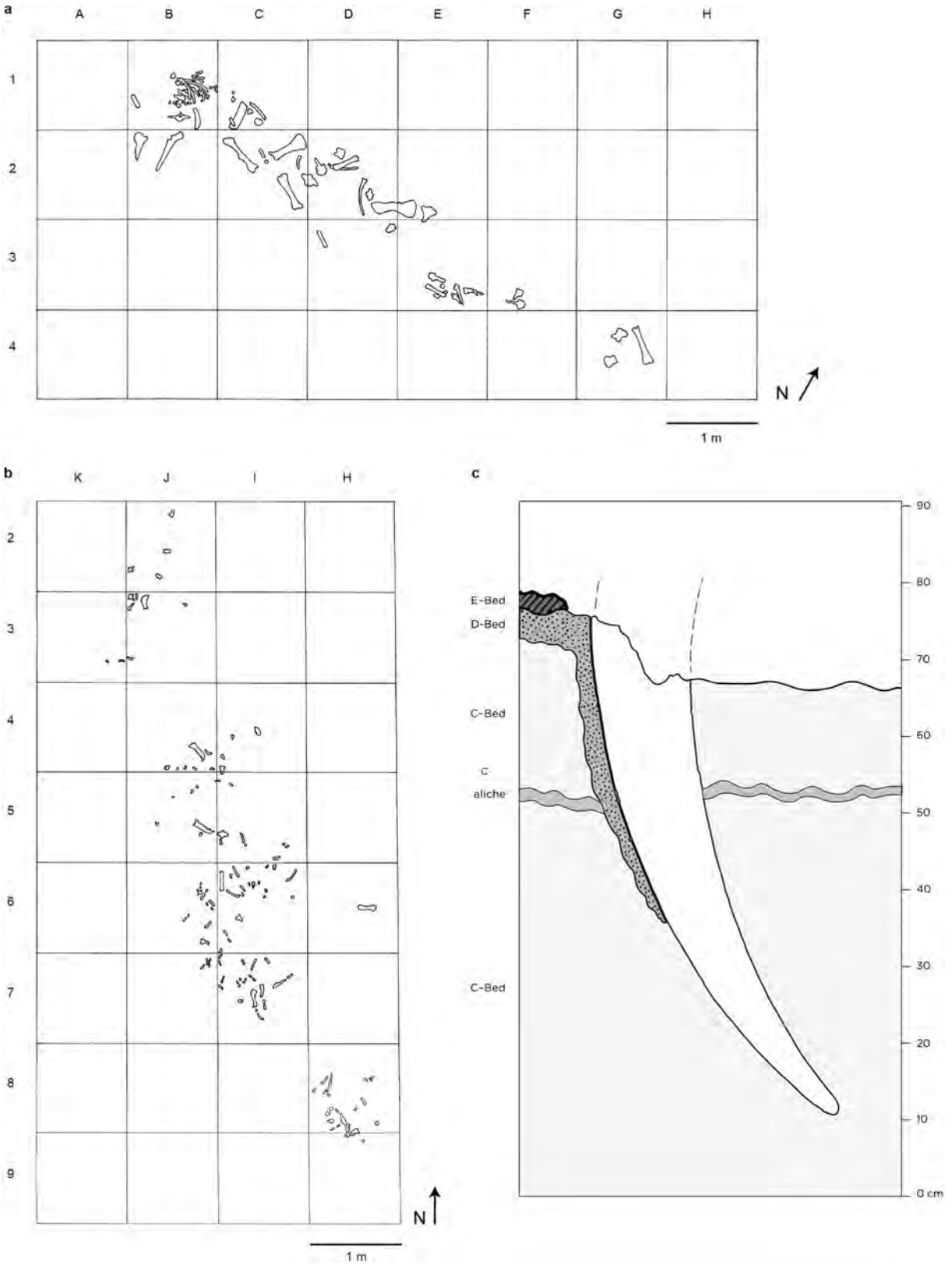

Extended Data Figure 7 | Pleistocene land mammal excavation grid maps and stratigraphic profile of *in situ* tusk. a, Partial horse skeleton (SDNHM 47731) recovered in Bed D. **b**, Partial dire wolf (SDNHM 49012) and deer excavation (SDNHM 49666) recovered in Bed D. Deer bones confined to grid units H8 and H9. **c**, Profile of vertically oriented mastodon tusk CM-56 recovered from grid unit B2. Note that the tusk extends from the level of Bed E into underlying Beds D and C through a caliche layer. Note the infilling of sediment from Bed D along the leading margin of the embedded tusk.

Extended Data Figure 8 | Experimental hammerstone percussion of elephant bone. a, Breakage of elephant femur in Tanzania (photograph provided by C. Musiba). **b**, Breakage of elephant femur in Colorado, USA. Note the spirally fractured bone fragment in mid-air near the right knee of the person holding the hammerstone (photograph provided by K. Alexander). **c**, Femur in **a** broken at mid-shaft. Smooth spiral fractures characteristic of green-bone breakage, attached cone flake (top left arrow) and broad arcuate percussion notch (bottom right arrow) (photograph provided by C. Musiba). **d**, Detached cone flakes produced by hammerstone on Colorado elephant femur. Arrows show cortical platforms and adjacent bulbs of percussion. **e**, Illustration showing radiating spiral fractures and impact point surrounded by cone flakes produced by hammerstone impact. **f**, Cross-section showing cone flakes formed around the impact point.

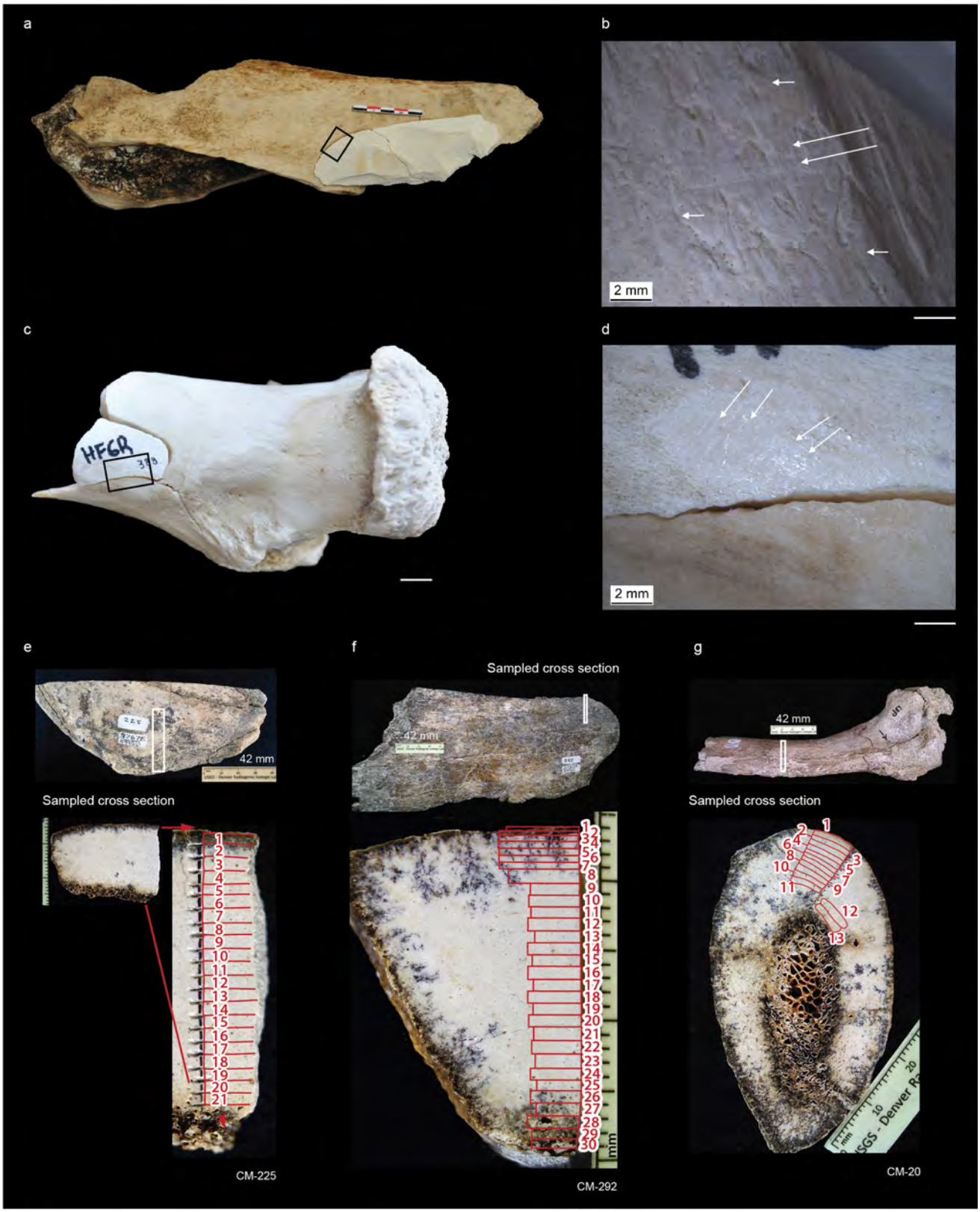

Extended Data Figure 9 | Experimentally produced anvil wear. **a**, **b**, Elephant femur broken on the cobble anvil by hammerstone percussion. **a**, Femur segment with refitting bone flakes. **b**, Close-up (square in **a**) of anvil polish on high points (short arrows) and striations (long arrows) (photograph provided by E. Duke). **c**, **d**, Cow femur broken on the cobble anvil by hammerstone percussion. **c**, Femur segment with refitted bone flake. Scale bar, 1 cm. **d**, Close-up (square in **c**) of anvil polish and striations (arrows) (photograph provided by E. Duke). **e**–**g**, CM bones used for radiometric analysis. Bone segments (CM-20, CM-225 and CM-292) and corresponding cross-sections subsampled for U-series dating profiles. Numbered red areas were subsampled by sequential micro-milling.

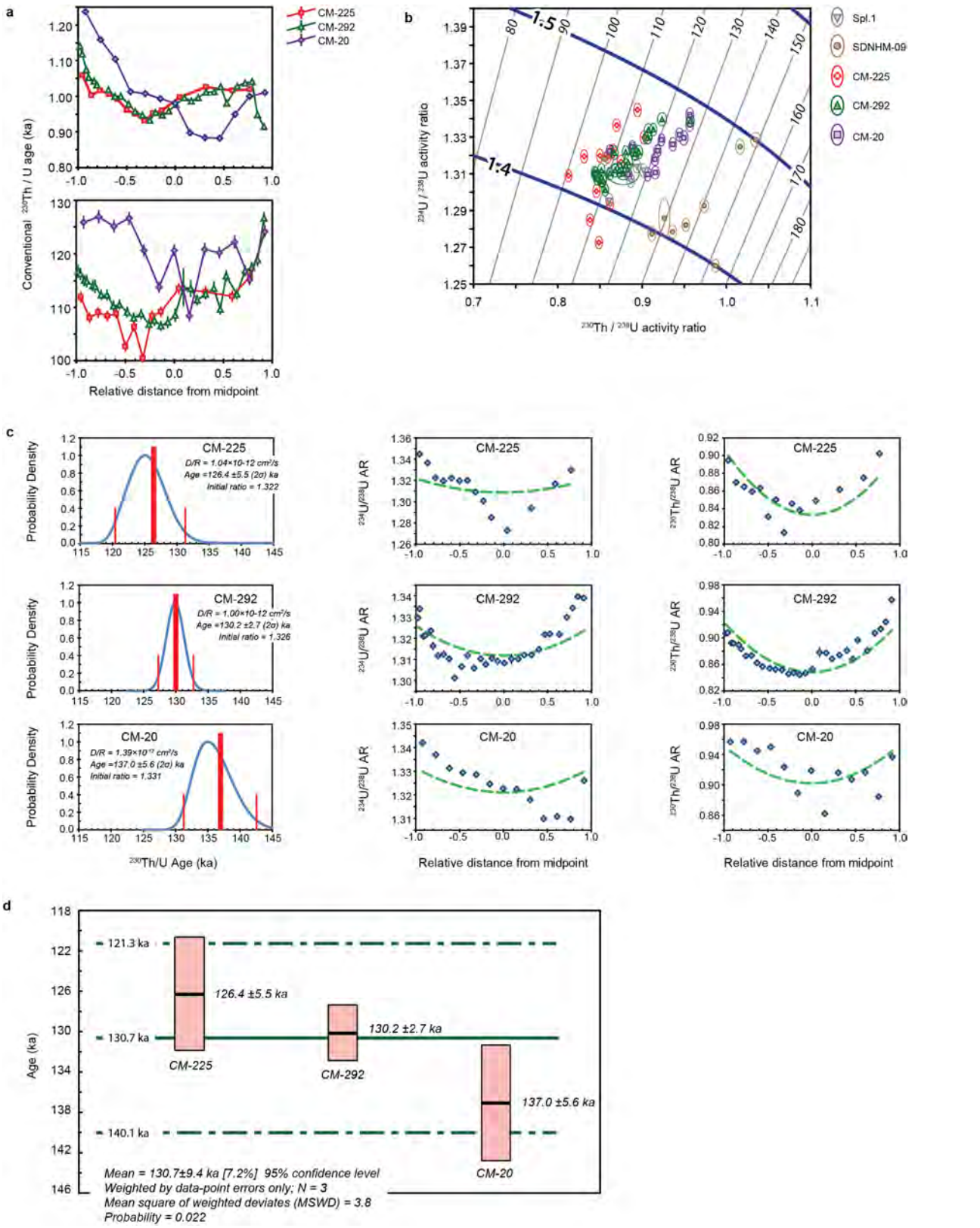

Extended Data Figure 10 | Results of U-series isotope analyses. See also Supplementary Table 12. **a**, Relative U concentrations and conventional ^{230}Th/U ages for profiles across three sections of cortical bone from samples CM-20 ($n = 13$), CM-225 ($n = 14$) and CM-292 ($n = 30$) plotted against relative distance from the midpoint of each section. **b**, U-series isotope-evolution plot showing measured activity ratios and error ellipses representing 2× s.d. (2σ), compositional paths for material with initial ^{234}U/^{238}U activity ratios of 1.4, 1.5 and 1.6 (dark curved lines), and isochrons labelled in ka. **c**, Results from diffusion–adsorption–decay (DAD) modelling of CM bone profiles using iDAD algorithms[30]. Left plots represent the marginal probability density function (blue curve) with maximum likelihood model age (thick vertical lines) and 95% credible interval half widths (thin vertical lines). Middle and right plots show individual ^{234}U/^{238}U and ^{230}Th/^{238}U activity ratios and maximum likelihood solutions for iDAD models (dashed lines). **d**, Best estimate of burial age of 130.7 ka (solid horizontal line) and 2σ uncertainties (±9.4 ka; dashed lines) determined as the mean of DAD dates for profiles shown in **c** weighted by their respective uncertainties.